Cell Reports

Article

Organoid-based drug screening reveals neddylation as therapeutic target for malignant rhabdoid tumors

Graphical abstract

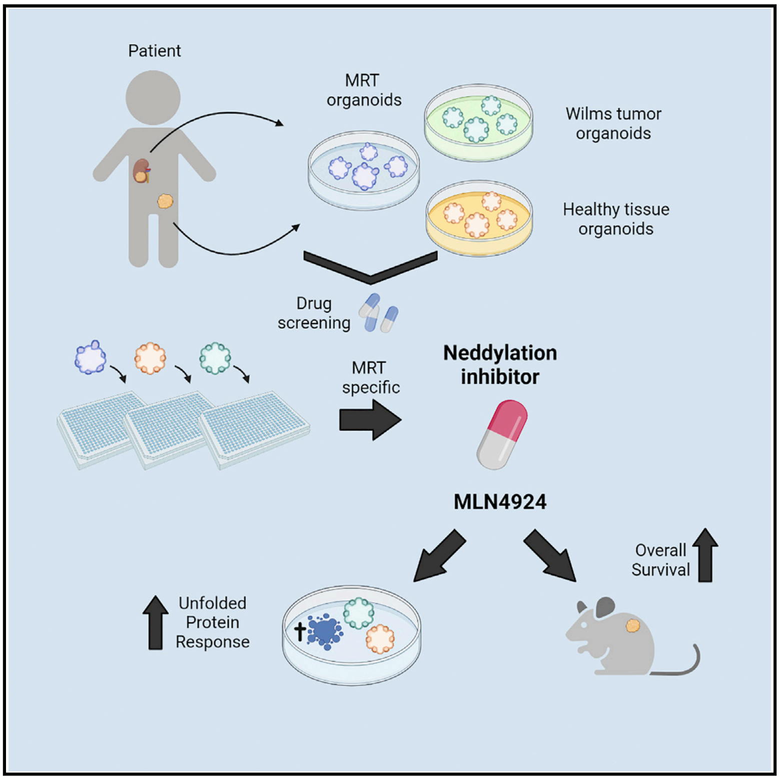

Authors

Camilla Calandrini, Sander R. van Hooff,
Irene Paassen, ...,
Marry M. van den Heuvel-Eibrink,
Jan J. Molenaar, Jarno Drost

Correspondence

j.drost@prinsesmaximacentrum.nl

In brief

Calandrini et al. identify neddylation as a therapeutic vulnerability for malignant rhabdoid tumors (MRTs), an aggressive and deadly childhood cancer. The neddylation inhibitor MLN4924 specifically induces cell death in MRTs *in vitro* and extends overall survival *in vivo*. Neddylation inhibition may, therefore, be a promising therapeutic strategy for MRTs.

Highlights

- Patient-derived organoids can be used to identify tumor-specific drug vulnerabilities
- Neddylation inhibitor MLN4924 is cytotoxic for malignant rhabdoid tumors (MRTs)
- MLN4924 induces apoptosis in MRTs via activation of the unfolded protein response
- Treatment with MLN4924 extends survival *in vivo* in an MRT PDX mouse model

Calandrini et al., 2021, Cell Reports *36*, 109568
August 24, 2021 © 2021 The Author(s).
https://doi.org/10.1016/j.celrep.2021.109568

Cell Reports

CellPress
OPEN ACCESS

Article

Organoid-based drug screening reveals neddylation as therapeutic target for malignant rhabdoid tumors

Camilla Calandrini,[1,2] Sander R. van Hooff,[1] Irene Paassen,[1,2] Dilara Ayyildiz,[1,2] Sepide Derakhshan,[1,2] M. Emmy M. Dolman,[1] Karin P.S. Langenberg,[1] Marieke van de Ven,[3] Cecilia de Heus,[4] Nalan Liv,[4] Marcel Kool,[1,5,6] Ronald R. de Krijger,[1,7] Godelieve A.M. Tytgat,[1] Marry M. van den Heuvel-Eibrink,[1] Jan J. Molenaar,[1] and Jarno Drost[1,2,8,*]

[1]Princess Máxima Center for Pediatric Oncology, Heidelberglaan 25, 3584 CS Utrecht, the Netherlands
[2]Oncode Institute, Heidelberglaan 25, 3584 CS Utrecht, the Netherlands
[3]Preclinical Intervention Unit of the Mouse Clinic for Cancer and Ageing (MCCA), NKI, Plesmanlaan 121, 1066 CX Amsterdam, the Netherlands
[4]Cell Biology, Center for Molecular Medicine, University Medical Center Utrecht, Heidelberglaan 100, 3584 CX Utrecht, the Netherlands
[5]Hopp Children's Cancer Center (KiTZ), 69120 Heidelberg, Germany
[6]Division of Pediatric Neurooncology, German Cancer Research Center DKFZ and German Cancer Consortium DKTK, 69120 Heidelberg, Germany
[7]University Medical Center, Department of Pathology, Heidelberglaan 100, 3584 CX Utrecht, the Netherlands
[8]Lead contact
*Correspondence: j.drost@prinsesmaximacentrum.nl

https://doi.org/10.1016/j.celrep.2021.109568

SUMMARY

Malignant rhabdoid tumors (MRTs) represent one of the most aggressive childhood malignancies. No effective treatment options are available, and prognosis is, therefore, dismal. Previous studies have demonstrated that tumor organoids capture the heterogeneity of patient tumors and can be used to predict patient response to therapy. Here, we perform drug screening on patient-derived normal and tumor organoids to identify MRT-specific therapeutic vulnerabilities. We identify neddylation inhibitor MLN4924 as a potential therapeutic agent. Mechanistically, we find increased neddylation in MRT organoids and tissues and show that MLN4924 induces a cytotoxic response via upregulation of the unfolded protein response. Lastly, we demonstrate *in vivo* efficacy in an MRT PDX mouse model, in which single-agent MLN4924 treatment significantly extends survival. Our study demonstrates that organoids can be used to find drugs selectively targeting tumor cells while leaving healthy cells unharmed and proposes neddylation inhibition as a therapeutic strategy in MRT.

INTRODUCTION

Malignant rhabdoid tumors (MRTs) are aggressive childhood tumors that occur in infants and young children (Weeks et al., 1989). They can arise in the brain (atypical teratoid rhabdoid tumor [ATRT]) as well as extracranially (kidney and soft tissues), where they are collectively called MRTs. MRTs are uniquely characterized by one common genetic driver event, bi-allelic loss of *SMARCB1* (95%) or *SMARCA4* (5%), key members of the SWI/SNF chromatin-remodeling complex (Biegel et al., 1999; Versteege et al., 1998). In addition, MRTs are considered genetically cold tumors with low mutational burden and a lack of chromosomal alterations (Chun et al., 2016; Lee et al., 2012). Therapy is multimodal, consisting of a combination of surgical intervention, radiotherapy, and heavy regimens of chemotherapy (Kerl et al., 2013). Despite that treatment, the prognosis remains dismal, with an overall survival of only ~25% (Reinhard et al., 2008). Furthermore, survivors suffer from side effects of the intense treatment regimen. MRTs, therefore, remain one of the big challenges in childhood cancer, and the identification of less-toxic therapeutic strategies is urgently needed.

The lack of physiologically relevant *in vitro* models has hampered therapeutic innovation in the MRT field. Patient-derived organoid models have emerged as robust pre-clinical models for cancer research (Drost and Clevers, 2018) and to be predictive of patient treatment response (Ganesh et al., 2019; Ooft et al., 2019; Tiriac et al., 2018; Vlachogiannis et al., 2018; Yao et al., 2020). We recently succeeded in generating patient-derived organoid models from MRTs of the kidney and demonstrated that these tumor organoids recapitulate the genetic, transcriptional, and DNA methylation profiles of the primary MRT tissue (Calandrini et al., 2020; Ooms et al., 2020).

Here, we set out to identify therapeutic agents for patients with MRT by performing drug screens on patient-derived MRT organoid cultures (kidneys and additional established cultures from extrarenal MRTs). By comparing the efficacy of the compounds in MRT to that of organoids derived from Wilms tumor and healthy tissues, we identified the neddylation inhibitor

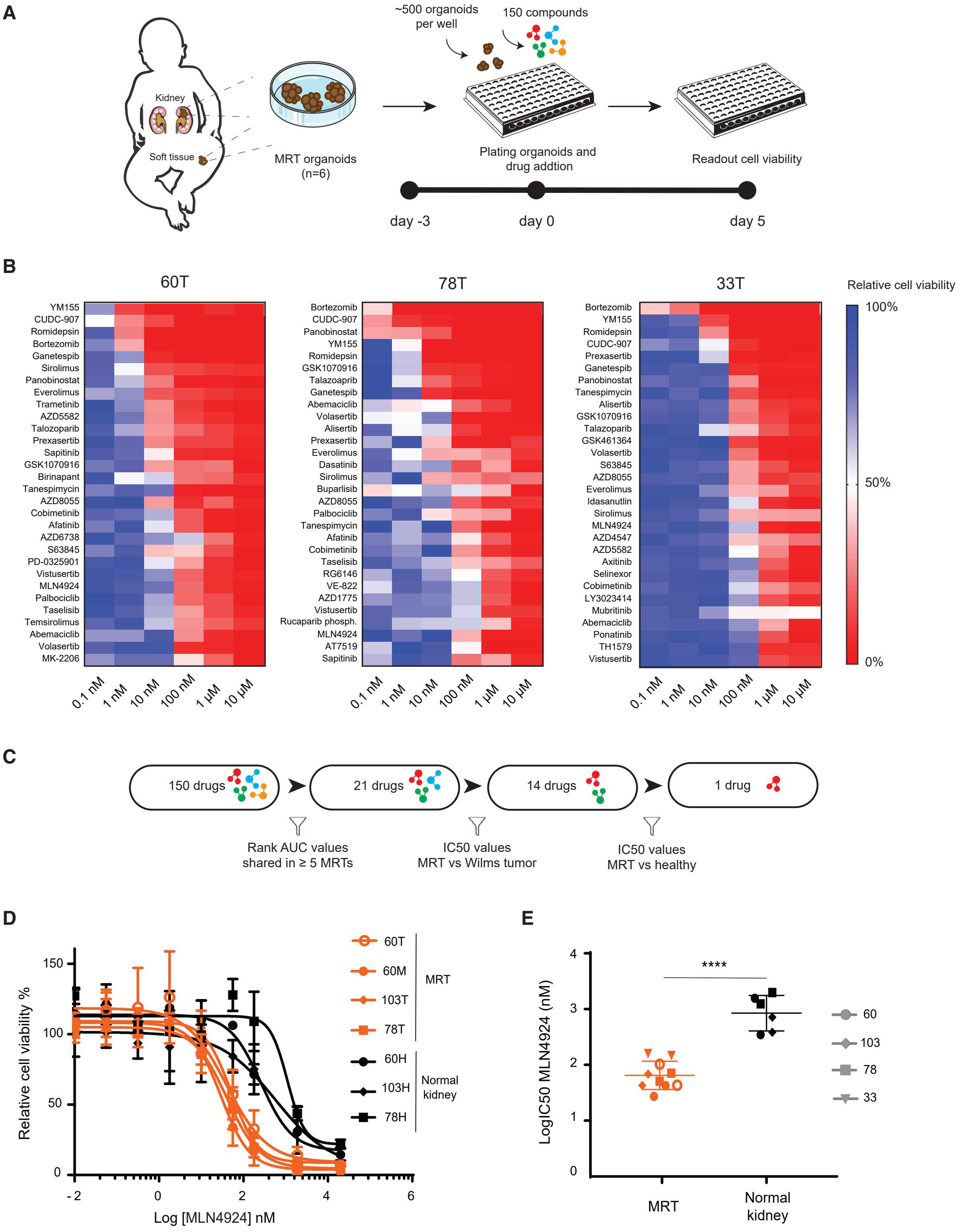

Figure 1. Drug screening of MRT organoids reveals tumor specific drug sensitivities

(A) Schematic overview of the organoid drug screening workflow.

(B) Compound screening of ~150 targeted drugs were performed on six patient-derived MRT organoid cultures (Figure S2A). The top-30 compounds are depicted ranked based on area under the curve (AUC) values for three representative MRT cultures. Color scale blue to red indicates decreasing ATP levels relative to DMSO control as a measure of cell viability.

(legend continued on next page)

MLN4924 as an MRT-specific vulnerability. MRT organoids demonstrate increased neddylation activity, which we confirmed in patient MRT tissues. Mechanistically, we suggest that this vulnerability is, at least partially, caused by increased endoplasmic reticulum (ER) stress and the activity of the unfolded protein response (UPR) in MRTs. In conclusion, we have identified neddylation inhibition as a promising therapeutic strategy for pediatric MRTs.

RESULTS

Drug screening of MRT organoids reveals tumor- and patient-specific drug sensitivities

To find therapeutic agents for MRTs, we used our previously described patient-derived MRT of the kidney organoid models (Calandrini et al., 2020) as a platform for drug screens. In addition, we included an additional established organoid model from an MRT growing in the pelvic area (Table S1). Extensive analyses revealed that the organoids have retained crucial characteristics of the parental tissue (Figures S1A–S1E), as we previously described for our MRTs of the kidney models (Calandrini et al., 2020; Chun et al., 2019). We screened a total of six MRT organoid lines derived from five patients with MRTs, including three primary tumors, one metastasis, and one case of patient-matching primary and metastatic tissue (Calandrini et al., 2020). We screened an in-house-developed drug library containing approximately 150 targeted compounds (Figure 1A; Table S2). Screening the library at six different concentrations allowed us to draw dose-response curves. We first selected targeted compounds that appeared most effective in at least five of six screened MRT organoid cultures based on the area under the curve (AUC) values (Figures 1B, S2A, and S2B), which yielded 21 compounds (Figure 1C). Next, we checked for MRT-specific activity of those compounds by comparing the half-maximal inhibitory concentration (IC_{50}) values of the selected drugs with the IC_{50} values of previously screened Wilms tumor organoids (Calandrini et al., 2020) (Figure S2C; Table S3). This yielded 14 drugs with more-potent efficacy on MRTs versus Wilms tumor organoids. Among those were drugs previously identified as potential therapies for MRTs, such as histone deacetylase (HDAC) inhibitors, HSP90 inhibitors, and the proteasome inhibitor bortezomib (Carugo et al., 2019; Muscat et al., 2016; Tran et al., 2020). We also identified multiple mTOR inhibitors, which we previously described as having a cytostatic effect in MRTs (Custers et al., 2021).

Despite their highly similar genetic-driver landscape, we found that some MRT cultures showed differential sensitivities toward specific drugs. For instance, organoid culture 78T was markedly less sensitive to the inhibitor of apoptosis (IAP) AZD5582 compared with that of other MRT organoid cultures (Figure S2D). No genetic cause could be identified in whole-genome sequencing (WGS) data of those cultures. Resistance to AZD5582 in pancreatic cancer models was previously linked to decreased expression of TNFR1 and TNFR2 (Moon et al., 2015). Using bulk RNA sequencing (RNA-seq) (Calandrini et al., 2020), we observed significantly reduced expression of both TNFR1 and TNFR2 in 78T compared with that of all other analyzed MRT organoids (Figure S2D). This may provide an explanation for the decreased sensitivity of 78T to AZD5582 and demonstrates that organoids can be used to find patient-specific drug vulnerabilities.

A drug showing efficacy in all tested MRT organoid cultures could be of therapeutic value for treatment of patients with MRTs. We identified MLN4924 as having a consistent IC_{50} value in all screened MRT organoid cultures, which was significantly less than the average IC_{50} value in Wilms tumor organoids (Figure S2C; Table S3). To further confirm the increased vulnerability of MRTs to MLN4924 treatment, we tested the effect of the drug on a panel of healthy-tissue-derived organoid lines. We included three patient-matching healthy kidney-tissue-derived organoids, as well as a small intestine and a hepatocyte-derived organoid culture (Drost et al., 2015; Hu et al., 2018; Schutgens et al., 2019) to test for potential nephrotoxicity, intestinal toxicity, and hepatotoxicity of MLN4924 treatment, respectively. Furthermore, we expanded the range of concentrations of MLN4924 to determine more-accurately the IC_{50} values for the different organoid lines. MRT organoids were markedly more sensitive to MLN4924 compared with patient-matching healthy kidney organoids and hepatocyte organoids (Figures 1D, 1E, and S2E; Table S4). Moreover, we measured an average IC_{50} value for MRT lines of ~75 nM, a concentration well below its reported maximum tolerated plasma dose in adult patients (Swords et al., 2018). Small-intestine organoids showed comparable sensitivity to MLN4924 as that of MRT organoids (Figure S2E). However, so far, no severe side effects related to the intestines have been reported during the first phases of clinical trial for MLN4924 (Nawrocki et al., 2012), which could potentially be explained by the high regenerative capacity of the intestinal lining.

Together, patient-derived MRT organoids can be used for drug testing, allowing us to find patient-specific drug vulnerabilities, as well as MLN4924, as a potentially promising targeted compound for MRT treatment.

Low-dose MLN4924 treatment induces apoptosis in MRT

To further characterize the drug-induced effects, we investigated whether MRT organoids can regrow after MLN4924 washout (Figure 2A). Three patient-derived MRT organoid lines with different growth rates were selected to conduct the experiment (Figure S3A). The mTOR inhibitor sirolimus and doxorubicin were included as controls because these drugs are known to have a cytostatic and cytotoxic effect on MRTs (Custers et al.,

(C) Schematic of the selection strategy to find MRT-specific drug vulnerabilities.

(D) Dose-response curves of MLN4924 for the indicated MRT and patient-matching healthy kidney-tissue-derived organoid cultures. Error bars represent SD of 2 independent experiments, each consisting of quadruplicate measurements.

(E) Average log(IC_{50}) values of MLN4924 in the indicated MRT- and patient-matching healthy kidney-organoid lines. Each value (two per organoid culture) represents the average of technical quadruplicates of an individual organoid culture. p values were calculated using a two-tailed unpaired Student's t test, two-sided. ****$p < 0.0001$.

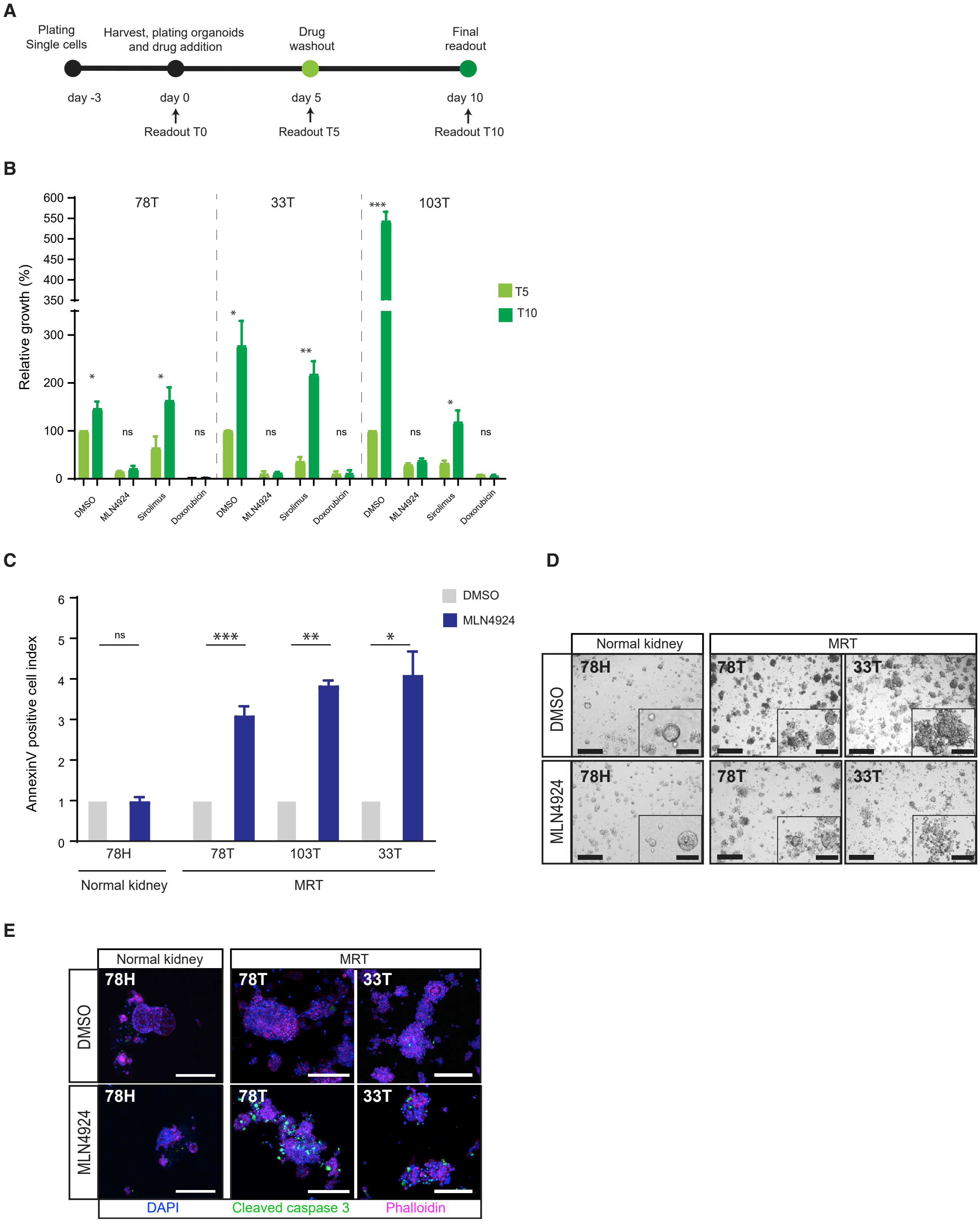

(legend on next page)

2021), respectively. Indeed, although significant regrowth was observed upon sirolimus withdrawal (Figures 2B and S3B), no regrowth occurred upon removal of doxorubicin (Figures 2B and S3B). Interestingly, no regrowth was observed upon MLN4924 washout in all three tested MRT lines, suggesting that MLN4924 treatment has a cytotoxic effect on MRT (Figures 2B and S3B). To further confirm that, we performed Annexin V/DAPI labeling upon treatment with MLN4924. Compared with the mock control as well as mTOR inhibition, a significant increase of apoptotic (i.e., Annexin V-positive) cells was observed upon MLN4924 treatment (Figures 2C, 2D, and S3C–S3F). Of note, no apoptotic response was observed upon MLN4924 treatment of patient-matching normal kidney organoids, again confirming an MRT-specific vulnerability (Figures 2C, 2D, S3C, and S3D). These results were further confirmed by immunofluorescence staining for cleaved caspase 3, demonstrating an increase in positively stained, apoptotic MRT organoids upon MLN4924 treatment compared with normal kidney organoids (Figure 2E). Overall, these findings suggest that MLN4924 has a cytotoxic effect in MRT, further substantiating its therapeutic potential.

MRTs demonstrate increased neddylation and a UPR-mediated apoptotic response upon MLN4924 treatment

Neddylation is a post-translational modification that regulates protein turnover via the conjugation of the ubiquitin-like protein NEDD8 to substrates in a three-step enzymatic process (Enchev et al., 2015; Kamitani et al., 1997). MLN4924 is a selective inhibitor of the neddylation-activating enzyme (NAE, enzyme E1), and its action hampers the overall neddylation process, resulting in cell-cycle arrest, apoptosis, or senescence in a cell-type-specific manner (Soucy et al., 2009). To investigate why MRTs show increased sensitivity toward MLN4924, we first analyzed the level of neddylation activity in MRT. Western blot analyses revealed strongly elevated levels of NEDD8 as well as neddylated proteins in MRT organoids compared with normal kidney and Wilms-tumor-derived organoids (Figures 3A and S3G). As expected, a strong downregulation of neddylated proteins was observed upon MLN4924 treatment in MRT samples (Figures 3A and S3G). Furthermore, and in line with previous reports (Godbersen et al., 2014; Jia et al., 2011; Knorr et al., 2015; Liu et al., 2017; Mackintosh et al., 2013), treatment with MLN4924 caused significant upregulation of the pro-apoptotic factor NOXA as well as cell-cycle regulators P21 and WEE1 (Figures S3H and S3I; Table S5). To confirm that the increase in protein neddylation observed in MRT organoids was not induced *in vitro*, we next performed immunohistochemistry for NEDD8 on patient tumor tissues. In line with the expression levels in organoids (Figure S3J), strong staining for NEDD8 was detected in MRT tissue (Figure 3B), whereas low or a complete lack of staining was observed in normal kidney and Wilms tumor tissue, respectively (Figure 3B). To find the potential cause of the increased neddylation in MRTs, we assessed mRNA expression levels of several E1 and E2 neddylation enzymes in MRTs, Wilms tumors, and normal kidney tissues and organoids (Calandrini et al., 2020; Schutgens et al., 2019). This revealed increased expression of *NAE1* (E1) and *UBE2M* (E2) enzymes in MRTs compared with Wilms tumor and/or normal kidney tissue and organoids (Figures 3C and 3D). We further corroborated these results by western blot (organoids) and immunohistochemistry analyses (tissues) (Figures 3E and S3K).

MRTs are typically driven by the inactivation of *SMARCB1* (Biegel et al., 1999; Versteege et al., 1998). Analyzing gene expression levels of E1 and E2 enzymes in MRT organoids in which *SMARCB1* expression was reconstituted by lentiviral transduction (Custers et al., 2021) revealed that mRNA levels of *NAE1* and *UBE2M*, the same enzymes we found to be specifically upregulated in MRTs (Figures 3C and 3D), were significantly downregulated upon *SMARCB1* re-expression (Figure 3F).

Together, our data show that MRTs demonstrate elevated neddylation, which is potentially caused by an increase in E1 and E2 enzyme expression driven by *SMARCB1* loss.

Recent reports have shown that blocking neddylation by treatment with MLN4924 activates UPR (Chen et al., 2016; McGrail et al., 2020), a cellular mechanism induced by ER stress and the consequent accumulation of misfolded proteins (Cao and Kaufman, 2012; Hetz, 2012). When cells are not able to alleviate severe ER stress, the UPR triggers an apoptotic response via the upregulation of the pro-apoptotic transcription factor CHOP (Chen et al., 2016). Interestingly, it has been reported that MRTs display enrichment for UPR gene expression compared with other tumor entities, suggesting that MRTs are characterized by baseline activation of the UPR (Carugo et al., 2019). By gene set enrichment analysis (GSEA) on bulk RNA-seq data (Calandrini et al., 2020), we confirmed that the UPR signature is significantly upregulated in MRT tissues and organoids as compared with Wilms tumors, pediatric renal cell carcinoma

---

Figure 2. Low-dose MLN4924 treatment induces apoptosis in MRTs

(A) Experimental overview of the drug-washout experiment.

(B) Bar graph represents cell viability of three MRT organoid lines at day 5 (T5) and day 10 (T10) relative to the DMSO control. 78T, 33T, and 103T MRT organoids were treated with either DMSO (vehicle), MLN4924 (100 nM; = IC_{70}), sirolimus (2 nM; = IC_{70}), or doxorubicin (100 nM; = IC_{70}). Data are represented as means ± SD (n = 3 independent experiments, each consisting of an average of three technical replicates). Regrowth was assessed by comparing T10 to T5 for each drug treatment. p values were calculated using a two-tailed unpaired Student's t test. $^{*}p < 0.05$, $^{**}p < 0.01$, $^{***}p < 0.001$. Representative brightfield pictures can be found in Figure S3B.

(C) Bar graph representing Annexin-V-positive cell indices of MRTs and normal kidney organoids upon treatment with 50 nM MLN4924 for 120 h. Annexin-V-positive cell-index values were calculated by normalizing apoptosis percentages to the respective DMSO vehicles. Data are represented as means ± SEM ($n \geq 3$ independent experiments). p values were calculated using a two-tailed unpaired Student's t test. $^{*}p < 0.05$, $^{**}p < 0.01$, $^{***}p < 0.001$. See also Figures S3C and S3D.

(D) Representative brightfield pictures of MRT and normal kidney organoids treated with DMSO vehicle or 50 nM MLN4924 for 120 h. Related to Figure 2C. Scale bars: 500 μm, zoom in: 150 μm.

(E) Immunofluorescence three-dimensional (3D) imaging of MRT and normal kidney organoids immunolabeled for cleaved caspase 3 (green), phalloidin (magenta), and DAPI (blue) after treatment with DMSO or 50 nM MLN4924 for 120 h. Scale bars: 250 μm.

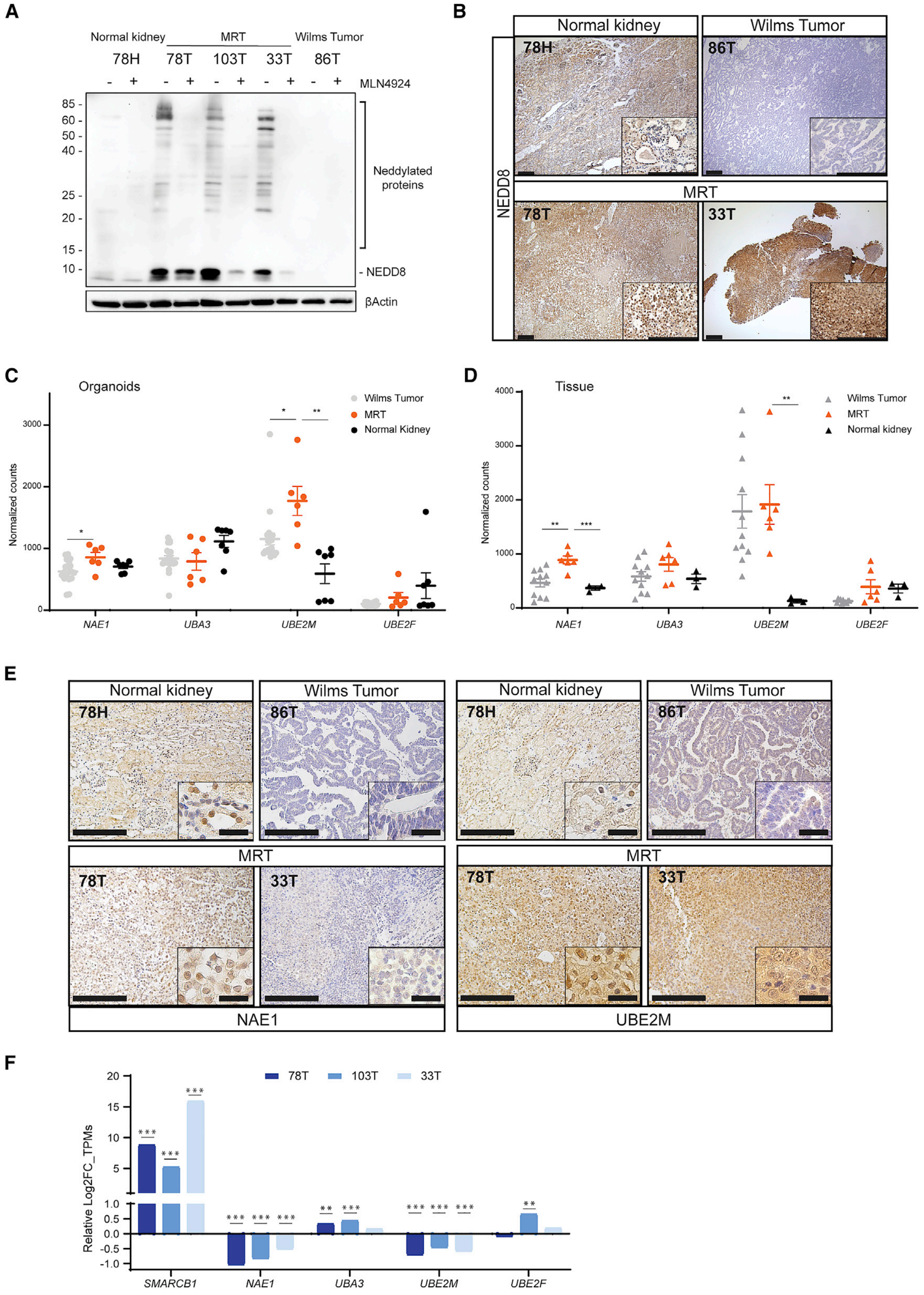

(legend on next page)

and normal kidney (Figures 4A–4D). To further validate the presence of ER stress and UPR response in MRTs, we performed transmission electron microscopy (TEM) on normal kidney and MRT organoid samples. Although kidney organoid cells showed a healthy-structured ER (Figures 4E, top left, and S3L), MRT cells displayed more, but thinner and fragmented, ER, accompanied by an increased presence of lipid droplets and helical ER filaments; altogether, these are signs of ER stress and UPR activation (Bernales et al., 2006; Carter et al., 2021; Ha et al., 2020; Li et al., 2008; Lu et al., 2020) (Figures 4E, top right, and S3L). Furthermore, we tested the effect of MLN4924 on MRT and normal kidney organoids by TEM. Although normal kidney organoids displayed minor signs of ER stress upon MLN4924 treatment, such as ER dilation, and a minor formation of lipid droplets (Figures 4E, bottom left, and S3L), MRT organoids presented with a dramatic accumulation of lipid droplets and extreme ER phenotypes (fragmented, disorganized, and enlarged; presence of helical fragments or completely missing ER) (Figures 4E, bottom right, and S3L). These MRT-specific phenotypes were also accompanied by the first signs of apoptosis and necrosis (Figure S3L).

To further corroborate the UPR-mediated apoptotic response in MRT upon MLN4924 treatment, we examined the expression of the downstream UPR effector CHOP in MRT organoids using qRT-PCR. Compared with the untreated control, significant upregulation of *CHOP* mRNA levels was observed in most of the tested MRT organoid lines upon treatment with MLN4924 (Figure 4F; Table S5). In addition to *CHOP* induction, we observed a significant induction of the apoptotic marker *BIM* (Figure 4F), previously described to be activated by CHOP in the UPR-mediated apoptotic response (Puthalakath et al., 2007).

Altogether, these results provide further evidence that MRT organoids experience ER stress and an UPR signature at baseline, which is further induced upon MLN4924 treatment.

MLN4924 inhibits MRT growth and increases survival *in vivo*

After demonstrating the efficacy of MLN4924 *in vitro*, we set out to investigate whether MLN4924 showed activity against MRT *in vivo*. For this purpose, we established an *in vivo* MRT xenograft model by subcutaneous injection of MRT organoids in immunocompromised mice, yielding tumors histologically recapitulating patient MRTs (Figure S4A).

To demonstrate *in vivo* efficacy of MLN4924 in MRT, we subcutaneously injected MRT organoids in immunocompromised mice and administered either vehicle or MLN4924 at 60 mg/kg BID for 5 weeks (five cycles of 5 days on/2 days off) when tumors reached a volume of ~250 mm^3 (Figure 5A) (Soucy et al., 2009). To demonstrate that the *in vitro* observed drug responses recapitulated the *in vivo* response, we also tested the effects of the mTOR inhibitor temsirolimus, showing a cytostatic effect *in vitro* (Figures 2B, S3B, S3E, and S3F; Custers et al. [2021]), in MRT xenografts (5 mg/kg for six cycles of 5 days on/2 days off for 6 weeks). Temsirolimus treatment resulted in a significantly decreased growth rate of the MRT tumors compared with vehicle-treated mice (Figure S4B). However, tumors still progressed under treatment, indicative of a cytostatic effect. Indeed, histological analysis of the tumors upon treatment termination revealed decreased proliferation and no apparent increase in apoptotic marker expression (Figure S4C). Instead, we observed significant shrinkage of tumor volume after two to three cycles of MLN4924 treatment, suggesting a cytotoxic effect of MLN4924 on MRT *in vivo* (Figures 5B and 5C). After that, tumor size remained stable during the course of the treatment. In line with that, no dramatic increase in the percentage of cleaved caspase-3-positive cells could be observed, possibly because the tumor size had stabilized at the time of harvesting the tumors (Figure S4D). Thus, the observed *in vitro* responses of MRT to mTOR and neddylation inhibition were recapitulated *in vivo*, further confirming the predictive value of *in vitro* organoid drug sensitivity for *in vivo* drug response. Furthermore, NEDD8 immunostaining on MRT tissues from vehicle- and MLN4924-treated mice showed a decrease in total NEDD8 levels in MLN4924-treated mice compared with vehicle, indicative of an on-target effect of the treatment (Figure S4E). Finally, mice treated with MLN4924 showed a significant increase in survival compared with vehicle-treated mice (Figure 5D). Histological characterization of kidneys, liver, small intestine, and body weight measurements did not reveal any signs of treatment-related toxicity in MLN4924-treated mice (Figures S5A–S5D).

In conclusion, using drug screens on patient-derived normal and tumor organoids, we found that the neddylation inhibitor MLN4924 inhibits MRT growth *in vitro* and *in vivo*, supporting future clinical investigation of this compound for the treatment of children with MRT.

Figure 3. MRT demonstrate increased neddylation activity

(A) Western blot analysis of NEDD8 and neddylated protein expression in the indicated organoid cultures treated for 120 h with 50 nM MLN4924 or DMSO. Bactin was included as a loading control. See also Figure S3G.

(B) NEDD8 immunostaining on normal kidney (top, left), Wilms tumor (top, right), and MRT tissues (bottom). Scale bars: 200 μm.

(C) Normalized counts of E1 (*NAE1* and *UBA3*) and E2 (*UBE2M* and *UBE2F*) enzymes involved in neddylation pathway. Data are represented as means ± SEM ($n \geq 7$). Depicted are values for MRT, Wilms tumor, and normal kidney derived organoids. p values were calculated using a two-tailed unpaired Student's t test. $^*p < 0.05$, $^{**}p < 0.01$.

(D) Same analysis as in (C) conducted on tissue samples. Data are represented as means ± SEM ($n \geq 3$). p values were calculated using a two-tailed unpaired Student's t test. $^*p < 0.05$, $^{**}p < 0.01$, $^{***}p < 0.001$.

(E) Immunostaining for enzyme NAE1 (left panel) and UBE2M (right panel) on normal kidney, Wilms tumor, and MRT tissues. Scale bars: 200 μm, zoom in: 25 μm.

(F) Log$_2$-fold change values of enzymes involved in neddylation pathway generated from three *SMARCB1*-reconstituted MRT organoid lines over respective luciferase controls. Log$_2$-fold change values were calculated using the R package DESeq2 starting from transcripts per kilobase million (TPM) values. Experiments were conducted in biological duplicates. Adjusted p values were calculated using the Wald significance test with multiple-testing corrections. $^{**}p < 0.01$, $^{***}p < 0.001$.

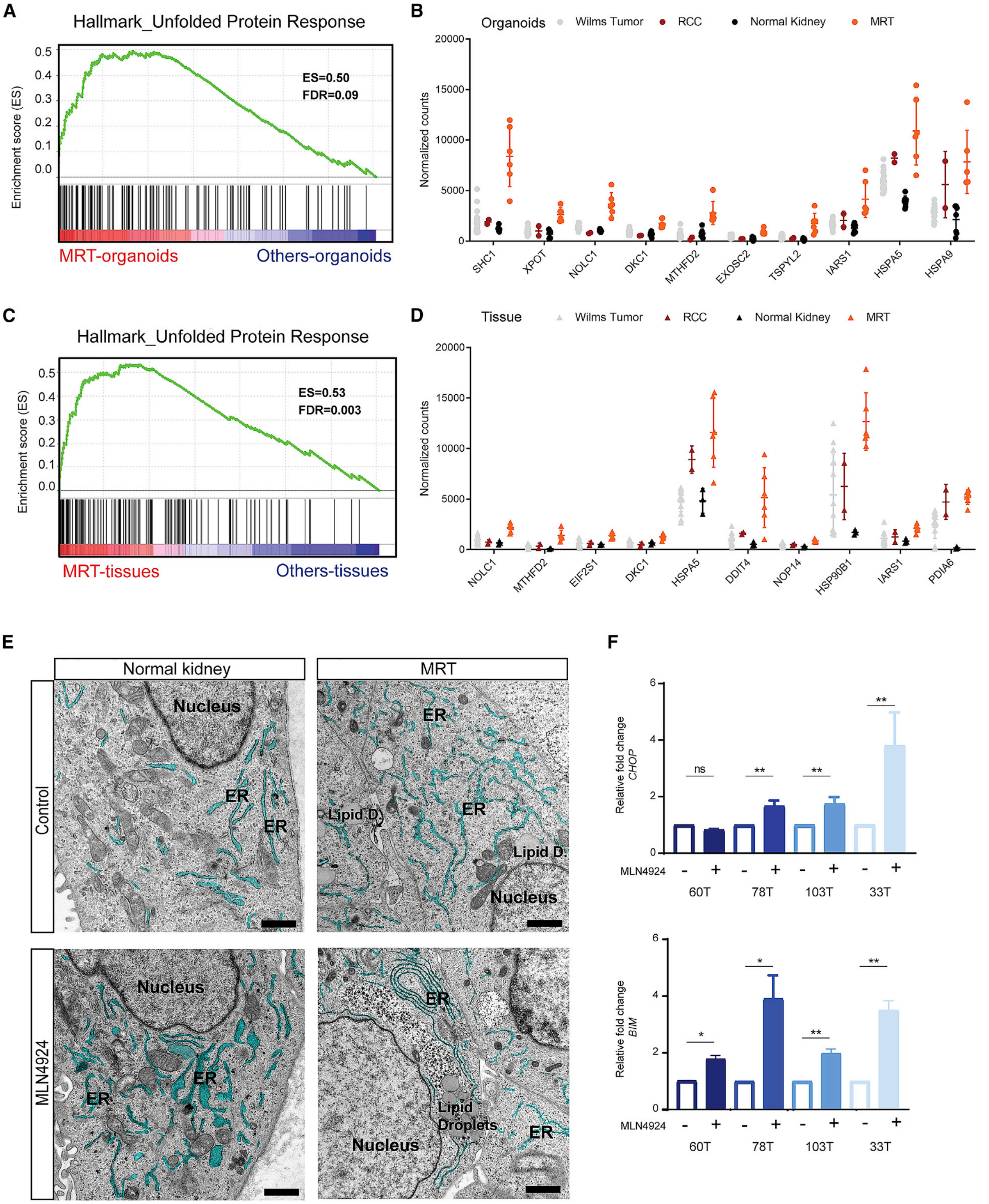

Figure 4. MLN4924 triggers a UPR-mediated apoptotic response

(A) GSEA on bulk RNA-seq data, demonstrating enrichment of UPR gene expression in MRT organoids versus Wilms tumor, renal cell carcinoma, and normal kidney organoids (MRT, n = 6; others, n = 30).

(legend continued on next page)

DISCUSSION

MRT is an aggressive and often fatal childhood malignancy. Even though patients are treated with intense multimodal therapy, in many cases, tumors become resistant to the treatment. In our study, we found that the neddylation inhibitor MLN4924 has a cytotoxic effect on MRTs specifically. We found an increased neddylation pathway and a UPR signature in MRT organoids and patient tissues, suggesting that neddylation might be an interesting therapeutic target in MRTs, which merits further evaluation. We confirmed our *in vitro* results with an *in vivo* study in an MRT PDX model generated by subcutaneous injection of MRT organoids. To exclude the *in vitro* organoid step from selecting for specific subpopulations of MRT cells, PDX models directly derived from patient tissues could be used. Moreover, tumor growth dynamics are known to be influenced by the microenvironment. Therefore, orthotopic MRT PDX models may provide a more-representative model than the widely used subcutaneous models. Lastly, PDX models of other tumor entities may be used to further test the MRT-specific effects of MLN4924.

Patient-derived organoids are a rapidly emerging model for studying cancer biology and identifying therapeutic targets (Drost and Clevers, 2018; Ooms et al., 2020). Growing organoids from healthy tissues and exploiting them for drug screening purposes in parallel with tumor organoids, potentially allows for the identification of therapeutic agents targeting tumor cells while leaving healthy cell unharmed (Vlachogiannis et al., 2018). Indeed, recent studies have demonstrated that kidney, hepatocytes, and oral mucosa organoids can be exploited for nephrotoxicity, hepatotoxicity, and oral toxicity testing, respectively (Driehuis et al., 2020; Meng, 2010; Takasato et al., 2015). Using a similar strategy, we screened kidney, hepatocytes, and small-intestine-derived organoids, which allowed us to find MRT-specific drug vulnerabilities, thereby limiting the possibility of toxic effects of MLN4924 in these healthy tissues.

MLN4924, or Pevonedistat, is currently being investigated in phase I–III clinical trials as a single agent (and in combination) for the treatment of different types of adult cancer (Sekeres et al., 2018; Zhao et al., 2014). Promising results from the phase I and II trials recently led to the initiation of the first trial of MLN4924 in pediatric solid and brain tumors, in combination with irinotecan and temozolomide (clinicaltrials.gov: NCT03323034). Our data suggest that monotherapy treatment with MLN4924 induces partial tumor regression but is likely not sufficient to induce complete tumor regression. Therefore, combining MLN4924 with other chemotherapeutic agents could be an interesting therapeutic strategy to explore further. Along the same lines, testing MLN4924 in combination with the current standard-of-care treatment could be of interest. Lastly, given the ability of MLN4924 to cross the blood brain barrier, neddylation inhibition could potentially be applied for the treatment of patients with atypical teratoid rhabdoid tumors (ATRTs) as well (Hua et al., 2015).

STAR★METHODS

Detailed methods are provided in the online version of this paper and include the following:

- KEY RESOURCES TABLE
- RESOURCE AVAILABILITY
  - ○ Lead contact
  - ○ Materials availability
  - ○ Data and code availability
- EXPERIMENTAL MODEL AND SUBJECT DETAILS
  - ○ Animals
  - ○ Patient-derived organoid lines
- METHOD DETAILS
  - ○ Whole genome sequencing and RNA sequencing
  - ○ DNA methylation profiling
  - ○ High throughput drug screening and validation
  - ○ Regrowth assay
  - ○ Annexin V/DAPI double staining
  - ○ Western blot
  - ○ Histology and immunohistochemistry
  - ○ 3D immunofluorescence staining
  - ○ Resin electron microscopy
  - ○ RNA isolation, cDNA preparation, and qRT-PCR
  - ○ *In vivo* drug study
- QUANTIFICATION AND STATISTICAL ANALYSIS

SUPPLEMENTAL INFORMATION

Supplemental information can be found online at https://doi.org/10.1016/j.celrep.2021.109568.

ACKNOWLEDGMENTS

We thank all the patients and their families for participating in the study. We thank the clinical team who facilitated our research. We are thankful to the Princess Máxima Center for Pediatric Oncology for high-throughput screening,

---

(B) Normalized counts of top-10 upregulated genes involved in the UPR as a result of the analysis described in (A). Data are represented as means ± SD ($n \geq 2$). Depicted are values for MRT, Wilms tumor, renal cell carcinoma, and normal kidney derived organoids.

(C) Same analysis as in (A), but in patient MRT tissues versus Wilms tumors, renal cell carcinoma, and normal kidney tissues (biological replicates: MRT, $n = 6$; others, $n = 16$).

(D) Normalized count of top-10 upregulated genes involved in the UPR as a result of the analysis described in (C). Data are represented as means ± SD ($n \geq 2$). Depicted are values for MRT, Wilms tumor, renal cell carcinoma, and normal kidney tissues.

(E) Representative TEM images of normal kidney and MRT organoids. (Top) Pictures of baseline/control status; (bottom) the effects of treatment with 50 nM MLN4924 for 48 h. Nuclei, ER, and lipid droplets are marked in the figure. The ER has been manually segmented and pseudo-colored for improved visualization (cyan). Scale bars: 500 nm. Additional images can be found in Figure S3L.

(F) Relative *CHOP* (top) and *BIM* (bottom) expression in four MRT organoid lines upon treatment with $1\ \mu M$ MLN4924 for 24 h, normalized to DMSO. Data are represented as means ± SD ($n \geq 3$ independent experiments, each consisting of an average of three technical replicates). p values were calculated using a two-tailed unpaired Student's t test. $^{*}p < 0.05$, $^{**}p < 0.01$.

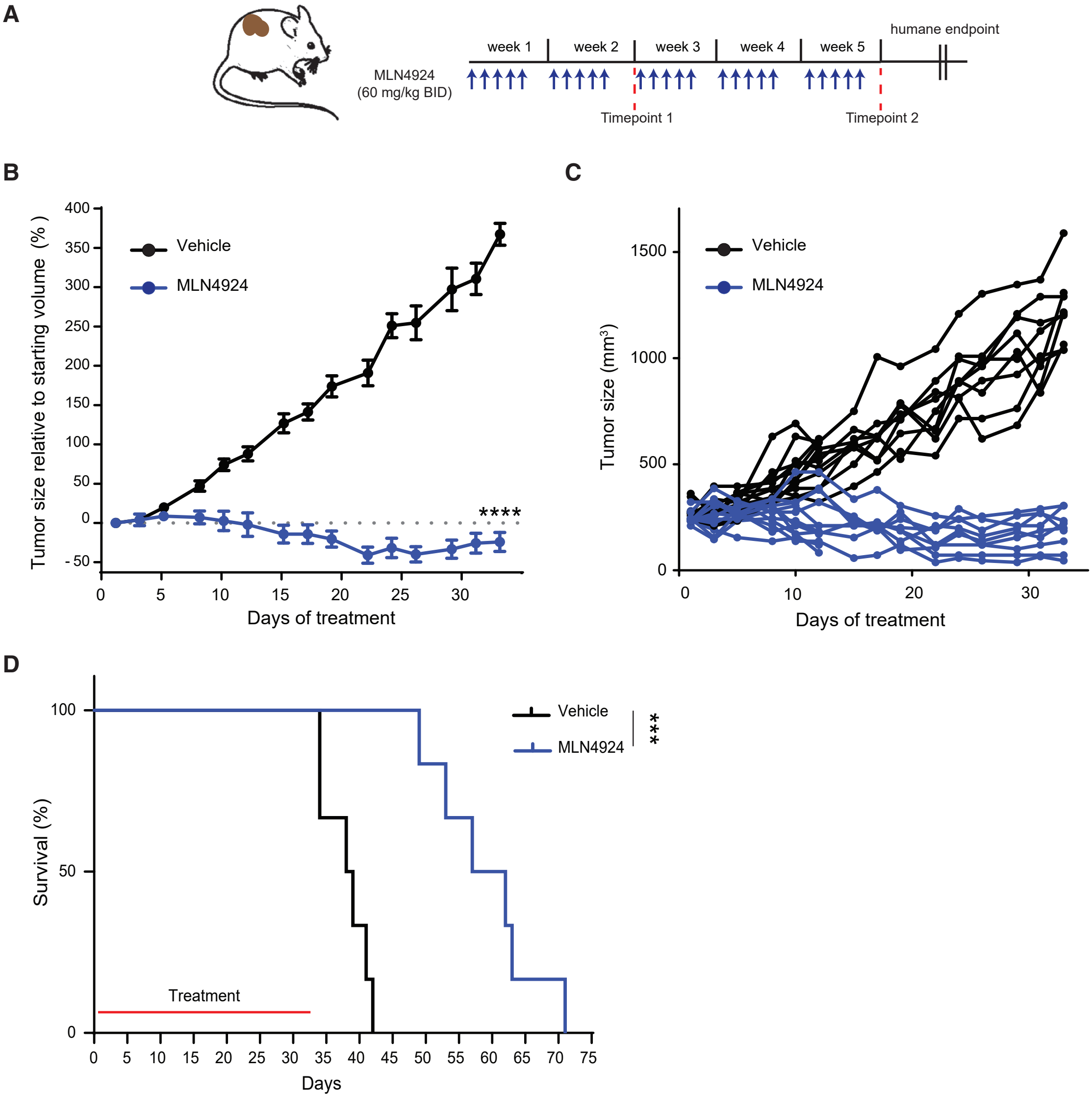

Figure 5. MLN4924 demonstrates *in vivo* efficacy in an MRT xenograft model

(A) Experimental overview of *in vivo* MLN4924 testing. Twenty-four mice (12 per experimental arm) bearing subcutaneous MRT tumors were injected with either 60 mg/kg BID MLN4924 or vehicle for a total of five cycles (5 days on, 2 days off), as previously described (Soucy et al., 2009). After completion of two cycles of treatment, as well as at the end of treatment, three mice per arm were sacrificed (time point, 1; time point, 2). The six mice left per arm were used for overall survival studies.

(B) MRT tumor growth in mice treated with either vehicle (black) or 60 mg/kg BID MLN4924 (blue) for up to five cycles. Values depicted are relative to the tumor volume at the start of treatment. Data are represented as means ± SEM (n = 12 until time point 1; n = 9 until time point 2). p value was calculated using a two-tailed unpaired Student's t test. ****$p < 0.0001$.

(C) MRT tumors volume for single mice in treatment as described in (B).

(D) Kaplan-Meier survival analysis of mice treated as described in (A). n = 6 mice per arm. p value was calculated using a two-tailed unpaired Student's t test. ***$p < 0.001$.

organoids, imaging, and fluorescence-activated cell sorting (FACS) facilities. We would like to thank the people from the Preclinical Intervention Unit of the Mouse Clinic for Cancer and Aging (MCCA) at the NKI for performing the *in vivo* studies. We thank Dr. Huili Hu and Prof. Dr. Hans Clevers for providing us with hepatocyte organoids. We are grateful for the support of the European Research Council (ERC) starting grant 850571 (J.D.), the Dutch Cancer Society (KWF)/Alpe d'HuZes Bas Mulder award (no. 10218, J.D. and S.D.), Oncode Institute, and Foundation Children Cancer Free (KiKa no. 292, C.C.). The graphical abstract was created with BioRender.com.

AUTHOR CONTRIBUTIONS

C.C. and J.D. designed and performed the experiments. C.C. and S.D. maintained the organoid cultures and performed the drug screens. M.E.M.D., K.P.S.L., and J.J.M. set up the drug-screening library. S.R.v.H. performed analyses of whole-genome sequencing and RNA sequencing data; I.P. performed and analyzed the *SMARCB1* re-expression experiment; D.A. and M.K. analyzed the DNA methylation data; M.v.d.V. performed and coordinated the *in vivo* experiments; N.L. and C.d.H. performed the TEM experiments and analyzed the electron microscopy images; R.R.d.K. performed histological evaluation of tumor organoids and tissues. G.A.M.T. and M.v.d.E. obtained informed consent from patients and established the pipeline to obtain tumor tissues. J.D. conceived the study, and J.D and C.C wrote the paper.

DECLARATION OF INTERESTS

The authors declare no competing interests.

Received: November 10, 2020
Revised: May 12, 2021
Accepted: July 28, 2021
Published: August 24, 2021

REFERENCES

Bernales, S., McDonald, K.L., and Walter, P. (2006). Autophagy counterbalances endoplasmic reticulum expansion during the unfolded protein response. PLoS Biol. *4*, e423.

Biegel, J.A., Zhou, J.-Y., Rorke, L.B., Stenstrom, C., Wainwright, L.M., and Fogelgren, B. (1999). Germ-line and acquired mutations of INI1 in atypical teratoid and rhabdoid tumors. Cancer Res. *59*, 74–79.

Calandrini, C., Schutgens, F., Oka, R., Margaritis, T., Candelli, T., Mathijsen, L., Ammerlaan, C., van Ineveld, R.L., Derakhshan, S., de Haan, S., et al. (2020). An organoid biobank for childhood kidney cancers that captures disease and tissue heterogeneity. Nat. Commun. *11*, 1310.

Cao, S.S., and Kaufman, R.J. (2012). Unfolded protein response. Curr. Biol. *22*, R622–R626.

Carter, S.D., Tran, N.-H., De Mazière, A., Ashkenazi, A., Klumperman, J., Jensen, G.J., and Walter, P. (2021). The stress-sensing domain of activated IRE1α forms helical filaments in narrow ER membrane tubes. bioRxiv, 2021.2002.2024.432779.

Carugo, A., Minelli, R., Sapio, L., Soeung, M., Carbone, F., Robinson, F.S., Tepper, J., Chen, Z., Lovisa, S., and Svelto, M. (2019). p53 is a master regulator of proteostasis in SMARCB1-deficient malignant rhabdoid tumors. Cancer Cell *35*, 204–220.e9.

Chen, P., Hu, T., Liang, Y., Li, P., Chen, X., Zhang, J., Ma, Y., Hao, Q., Wang, J., Zhang, P., et al. (2016). Neddylation inhibition activates the extrinsic apoptosis pathway through ATF4–CHOP–DR5 axis in human esophageal cancer cells. Clin. Cancer Res. *22*, 4145–4157.

Chun, H.E., Lim, E.L., Heravi-Moussavi, A., Saberi, S., Mungall, K.L., Bilenky, M., Carles, A., Tse, K., Shlafman, I., Zhu, K., et al. (2016). Genome-wide profiles of extra-cranial malignant rhabdoid tumors reveal heterogeneity and dysregulated developmental pathways. Cancer Cell *29*, 394–406.

Chun, H.-J.E., Johann, P.D., Milne, K., Zapatka, M., Buellesbach, A., Ishaque, N., Iskar, M., Erkek, S., Wei, L., and Tessier-Cloutier, B. (2019). Identification and analyses of extra-cranial and cranial rhabdoid tumor molecular subgroups reveal tumors with cytotoxic T cell infiltration. Cell Rep. *29*, 2338–2354.e7.

Custers, L., Khabirova, E., Coorens, T.H.H., Oliver, T.R.W., Calandrini, C., Young, M.D., Vieira Braga, F.A., Ellis, P., Mamanova, L., Segers, H., et al. (2021). Somatic mutations and single-cell transcriptomes reveal the root of malignant rhabdoid tumours. Nat. Commun. *12*, 1407.

Dekkers, J.F., Alieva, M., Wellens, L.M., Ariese, H.C.R., Jamieson, P.R., Vonk, A.M., Amatngalim, G.D., Hu, H., Oost, K.C., Snippert, H.J.G., et al. (2019). High-resolution 3D imaging of fixed and cleared organoids. Nat. Protoc. *14*, 1756–1771.

Delannoy, A., Wilhelm, E., Eilebrecht, S., Alvarado-Cuevas, E.M., Benecke, A.G., and Bell, B. (2018). BIM and NOXA are mitochondrial effectors of TAF6δ-driven apoptosis. Cell Death Dis. *9*, 70.

Driehuis, E., Oosterom, N., Heil, S.G., Muller, I.B., Lin, M., Kolders, S., Jansen, G., de Jonge, R., Pieters, R., Clevers, H., and van den Heuvel-Eibrink, M.M. (2020). Patient-derived oral mucosa organoids as an in vitro model for methotrexate induced toxicity in pediatric acute lymphoblastic leukemia. PLoS ONE *15*, e0231588.

Drost, J., and Clevers, H. (2018). Organoids in cancer research. Nat. Rev. Cancer *18*, 407–418.

Drost, J., Mantovani, F., Tocco, F., Elkon, R., Comel, A., Holstege, H., Kerkhoven, R., Jonkers, J., Voorhoeve, P.M., Agami, R., and Del Sal, G. (2010). BRD7 is a candidate tumour suppressor gene required for p53 function. Nat. Cell Biol. *12*, 380–389.

Drost, J., van Jaarsveld, R.H., Ponsioen, B., Zimberlin, C., van Boxtel, R., Buijs, A., Sachs, N., Overmeer, R.M., Offerhaus, G.J., Begthel, H., et al. (2015). Sequential cancer mutations in cultured human intestinal stem cells. Nature *521*, 43–47.

Enchev, R.I., Schulman, B.A., and Peter, M. (2015). Protein neddylation: beyond cullin-RING ligases. Nat. Rev. Mol. Cell Biol. *16*, 30–44.

Ganesh, K., Wu, C., O'Rourke, K.P., Szeglin, B.C., Zheng, Y., Sauvé, C.G., Adileh, M., Wasserman, I., Marco, M.R., Kim, A.S., et al. (2019). A rectal cancer organoid platform to study individual responses to chemoradiation. Nat. Med. *25*, 1607–1614.

Godbersen, J.C., Humphries, L.A., Danilova, O.V., Kebbekus, P.E., Brown, J.R., Eastman, A., and Danilov, A.V. (2014). The Nedd8-activating enzyme inhibitor MLN4924 thwarts microenvironment-driven NF-κB activation and induces apoptosis in chronic lymphocytic leukemia B cells. Clin. Cancer Res. *20*, 1576–1589.

Ha, T.W., Jeong, J.H., Shin, H., Kim, H.K., Im, J.S., Song, B.H., Hanna, J., Oh, J.S., Woo, D.-H., Han, J., and Lee, M.R. (2020). Characterization of endoplasmic reticulum (ER) in human pluripotent stem cells revealed increased susceptibility to cell death upon ER stress. Cells *9*, 1078.

Hetz, C. (2012). The unfolded protein response: controlling cell fate decisions under ER stress and beyond. Nat. Rev. Mol. Cell Biol. *13*, 89–102.

Hu, H., Gehart, H., Artegiani, B., Löpez-Iglesias, C., Dekkers, F., Basak, O., van Es, J., Chuva de Sousa Lopes, S.M., Begthel, H., Korving, J., et al. (2018). Long-term expansion of functional mouse and human hepatocytes as 3D organoids. Cell *175*, 1591–1606.e19.

Hua, W., Li, C., Yang, Z., Li, L., Jiang, Y., Yu, G., Zhu, W., Liu, Z., Duan, S., Chu, Y., et al. (2015). Suppression of glioblastoma by targeting the overactivated protein neddylation pathway. Neuro-oncol. *17*, 1333–1343.

Jia, L., Li, H., and Sun, Y. (2011). Induction of p21-dependent senescence by an NAE inhibitor, MLN4924, as a mechanism of growth suppression. Neoplasia *13*, 561–569.

John, C.R., Watson, D., Russ, D., Goldmann, K., Ehrenstein, M., Pitzalis, C., Lewis, M., and Barnes, M. (2020). M3C: Monte Carlo reference-based consensus clustering. Sci. Rep. *10*, 1816.

Kamitani, T., Kito, K., Nguyen, H.P., and Yeh, E.T. (1997). Characterization of NEDD8, a developmentally down-regulated ubiquitin-like protein. J. Biol. Chem. *272*, 28557–28562.

Kerl, K., Holsten, T., and Frühwald, M.C. (2013). Rhabdoid tumors: clinical approaches and molecular targets for innovative therapy. Pediatr. Hematol. Oncol. *30*, 587–604.

Knorr, K.L., Schneider, P.A., Meng, X.W., Dai, H., Smith, B.D., Hess, A.D., Karp, J.E., and Kaufmann, S.H. (2015). MLN4924 induces Noxa upregulation in acute myelogenous leukemia and synergizes with Bcl-2 inhibitors. Cell Death Differ. *22*, 2133–2142.

Lee, R.S., Stewart, C., Carter, S.L., Ambrogio, L., Cibulskis, K., Sougnez, C., Lawrence, M.S., Auclair, D., Mora, J., Golub, T.R., et al. (2012). A remarkably simple genome underlies highly malignant pediatric rhabdoid cancers. J. Clin. Invest. *122*, 2983–2988.

Li, J., Ni, M., Lee, B., Barron, E., Hinton, D.R., and Lee, A.S. (2008). The unfolded protein response regulator GRP78/BiP is required for endoplasmic reticulum integrity and stress-induced autophagy in mammalian cells. Cell Death Differ. *15*, 1460–1471.

Liu, X., Jiang, Y., Wu, J., Zhang, W., Liang, Y., Jia, L., Yu, J., Jeong, L.S., and Li, L. (2017). NEDD8-activating enzyme inhibitor, MLN4924 (Pevonedistat) induces NOXA-dependent apoptosis through up-regulation of ATF-4. Biochem. Biophys. Res. Commun. *488*, 1–5.

Love, M.I., Huber, W., and Anders, S. (2014). Moderated estimation of fold change and dispersion for RNA-seq data with DESeq2. Genome Biol. *15*, 550.

Lu, M., van Tartwijk, F.W., Lin, J.Q., Nijenhuis, W., Parutto, P., Fantham, M., Christensen, C.N., Avezov, E., Holt, C.E., Tunnacliffe, A., et al. (2020). The structure and global distribution of the endoplasmic reticulum network are actively regulated by lysosomes. Sci. Adv. *6*, eabc7209.

Mackintosh, C., García-Domínguez, D.J., Ordóñez, J.L., Ginel-Picardo, A., Smith, P.G., Sacristán, M.P., and de Álava, E. (2013). WEE1 accumulation and deregulation of S-phase proteins mediate MLN4924 potent inhibitory effect on Ewing sarcoma cells. Oncogene *32*, 1441–1451.

McGrail, D.J., Garnett, J., Yin, J., Dai, H., Shih, D.J.H., Lam, T.N.A., Li, Y., Sun, C., Li, Y., Schmandt, R., et al. (2020). Proteome instability is a therapeutic vulnerability in mismatch repair-deficient cancer. Cancer Cell *37*, 371–386.e12.

Meng, Q. (2010). Three-dimensional culture of hepatocytes for prediction of drug-induced hepatotoxicity. Expert Opin. Drug Metab. Toxicol. *6*, 733–746.

Moon, J.-H., Shin, J.-S., Hong, S.-W., Jung, S.-A., Hwang, I.-Y., Kim, J.H., Choi, E.K., Ha, S.-H., Kim, J.-S., Kim, K.-M., et al. (2015). A novel small-molecule IAP antagonist, AZD5582, draws Mcl-1 down-regulation for induction of apoptosis through targeting of cIAP1 and XIAP in human pancreatic cancer. Oncotarget *6*, 26895–26908.

Muscat, A., Popovski, D., Jayasekara, W.S.N., Rossello, F.J., Ferguson, M., Marini, K.D., Alamgeer, M., Algar, E.M., Downie, P., Watkins, D.N., et al. (2016). Low-dose histone deacetylase inhibitor treatment leads to tumor growth arrest and multi-lineage differentiation of malignant rhabdoid tumors. Clin. Cancer Res. *22*, 3560–3570.

Nawrocki, S.T., Griffin, P., Kelly, K.R., and Carew, J.S. (2012). MLN4924: a novel first-in-class inhibitor of NEDD8-activating enzyme for cancer therapy. Expert Opin. Investig. Drugs *21*, 1563–1573.

Ooft, S.N., Weeber, F., Dijkstra, K.K., McLean, C.M., Kaing, S., van Werkhoven, E., Schipper, L., Hoes, L., Vis, D.J., van de Haar, J., et al. (2019). Patient-derived organoids can predict response to chemotherapy in metastatic colorectal cancer patients. Sci. Transl. Med. *11*, eaay2574.

Ooms, A.H.A.G., Calandrini, C., de Krijger, R.R., and Drost, J. (2020). Organoid models of childhood kidney tumours. Nat. Rev. Urol. *17*, 311–313.

Puthalakath, H., O'Reilly, L.A., Gunn, P., Lee, L., Kelly, P.N., Huntington, N.D., Hughes, P.D., Michalak, E.M., McKimm-Breschkin, J., Motoyama, N., et al. (2007). ER stress triggers apoptosis by activating BH3-only protein Bim. Cell *129*, 1337–1349.

Reinhard, H., Reinert, J., Beier, R., Furtwängler, R., Alkasser, M., Rutkowski, S., Frühwald, M., Koscielniak, E., Leuschner, I., Kaatsch, P., and Graf, N. (2008). Rhabdoid tumors in children: prognostic factors in 70 patients diagnosed in Germany. Oncol. Rep. *19*, 819–823.

Schutgens, F., Rookmaaker, M.B., Margaritis, T., Rios, A., Ammerlaan, C., Jansen, J., Gijzen, L., Vormann, M., Vonk, A., Viveen, M., et al. (2019). Tubuloids derived from human adult kidney and urine for personalized disease modeling. Nat. Biotechnol. *37*, 303–313.

Sekeres, M.A., Fram, R.J., Hua, Z., and Ades, L. (2018). Phase 3 study of first line pevonedistat (PEV) + azacitidine (AZA) versus single-agent AZA in patients with higher-risk myelodysplastic syndromes (HR MDS), chronic myelomonocytic leukemia (CMML) or low-blast acute myelogenous leukemia (AML). J. Clin. Oncol. *36* (*suppl*), TPS7077.

Soucy, T.A., Smith, P.G., Milhollen, M.A., Berger, A.J., Gavin, J.M., Adhikari, S., Brownell, J.E., Burke, K.E., Cardin, D.P., Critchley, S., et al. (2009). An inhibitor of NEDD8-activating enzyme as a new approach to treat cancer. Nature *458*, 732–736.

Swords, R.T., Coutre, S., Maris, M.B., Zeidner, J.F., Foran, J.M., Cruz, J., Erba, H.P., Berdeja, J.G., Tam, W., Vardhanabhuti, S., et al. (2018). Pevonedistat, a first-in-class NEDD8-activating enzyme inhibitor, combined with azacitidine in patients with AML. Blood *131*, 1415–1424.

Takasato, M., Er, P.X., Chiu, H.S., Maier, B., Baillie, G.J., Ferguson, C., Parton, R.G., Wolvetang, E.J., Roost, M.S., Chuva de Sousa Lopes, S.M., and Little, M.H. (2015). Kidney organoids from human iPS cells contain multiple lineages and model human nephrogenesis. Nature *526*, 564–568.

Tiriac, H., Belleau, P., Engle, D.D., Plenker, D., Deschênes, A., Somerville, T.D.D., Froeling, F.E.M., Burkhart, R.A., Denroche, R.E., Jang, G.-H., et al. (2018). Organoid profiling identifies common responders to chemotherapy in pancreatic cancer. Cancer Discov. *8*, 1112–1129.

Toral, M., Jiménez, R., Romero, M., Robles-Vera, I., Sánchez, M., Salaices, M., Sabio, J.M., and Duarte, J. (2017). Role of endoplasmic reticulum stress in the protective effects of PPARβ/δ activation on endothelial dysfunction induced by plasma from patients with lupus. Arthritis Res. Ther. *19*, 268.

Tran, H.M., Wu, K.-S., Sung, S.-Y., Changou, C.A., Hsieh, T.-H., Liu, Y.-R., Liu, Y.-L., Tsai, M.-L., Lee, H.-L., Hsieh, K.L.-C., et al. (2020). Upregulation of protein synthesis and proteasome degradation confers sensitivity to proteasome inhibitor bortezomib in myc-atypical teratoid/rhabdoid tumors. Cancers (Basel) *12*, 752.

Vandesompele, J., De Preter, K., Pattyn, F., Poppe, B., Van Roy, N., De Paepe, A., and Speleman, F. (2002). Accurate normalization of real-time quantitative RT-PCR data by geometric averaging of multiple internal control genes. Genome Biol. *3*, H0034.

Versteege, I., Sévenet, N., Lange, J., Rousseau-Merck, M.-F., Ambros, P., Handgretinger, R., Aurias, A., and Delattre, O. (1998). Truncating mutations of hSNF5/INI1 in aggressive paediatric cancer. Nature *394*, 203–206.

Vlachogiannis, G., Hedayat, S., Vatsiou, A., Jamin, Y., Fernández-Mateos, J., Khan, K., Lampis, A., Eason, K., Huntingford, I., Burke, R., et al. (2018). Patient-derived organoids model treatment response of metastatic gastrointestinal cancers. Science *359*, 920–926.

Wang, X., Zhang, W., Yan, Z., Liang, Y., Li, L., Yu, X., Feng, Y., Fu, S., Zhang, Y., Zhao, H., et al. (2016). Radiosensitization by the investigational NEDD8-activating enzyme inhibitor MLN4924 (pevonedistat) in hormone-resistant prostate cancer cells. Oncotarget *7*, 38380–38391.

Weeks, D.A., Beckwith, J.B., Mierau, G.W., and Luckey, D.W. (1989). Rhabdoid tumor of kidney: a report of 111 cases from the National Wilms' Tumor Study Pathology Center. Am. J. Surg. Pathol. *13*, 439–458.

Worst, B.C., van Tilburg, C.M., Balasubramanian, G.P., Fiesel, P., Witt, R., Freitag, A., Boudalil, M., Previti, C., Wolf, S., Schmidt, S., et al. (2016). Next-generation personalised medicine for high-risk paediatric cancer patients - The INFORM pilot study. Eur. J. Cancer *65*, 91–101.

Yao, Y., Xu, X., Yang, L., Zhu, J., Wan, J., Shen, L., Xia, F., Fu, G., Deng, Y., Pan, M., et al. (2020). Patient-derived organoids predict chemoradiation responses of locally advanced rectal cancer. Cell Stem Cell *26*, 17–26.e6.

Zhao, Y., Morgan, M.A., and Sun, Y. (2014). Targeting neddylation pathways to inactivate cullin-RING ligases for anticancer therapy. Antioxid. Redox Signal. *21*, 2383–2400.

STAR★METHODS

KEY RESOURCES TABLE

REAGENT or RESOURCE	SOURCE	IDENTIFIER
Antibodies		
APC-AnnexinV	BD Biosciences	Cat# 550475; RRID:AB_2868885
NEDD8	Cell Signaling Technology	Cat #2754; RRID:AB_659972
GAPDH	Abcam	ab-9485; RRID: AB_307275
βActin	Abcam	ab-6276; RRID:AB_2223210
CHOP	Cell Signaling Technology	Cat #2895; RRID:AB_2089254
NAE1	Thermo Fisher	Cat #PA5-59836; RRID:AB_2644435
UBE2M	Abcam	ab-109507; RRID:AB_10892148
Cleaved caspase 3	Cell Signaling Technology	Cat #9661; RRID:AB_2341188
Alexa Fluor 647 phalloidin	Thermo Fisher	Cat# A22287; RRID:AB_2620155
WEE1	Santa Cruz	#SC5285; RRID:AB_628447
P21	Santa Cruz	#SC6246; RRID:AB_628073
Ki67	Monosan	MONX10283; RRID:AB_1833494
DAPI	Thermo Fisher	Cat# D1306; RRID:AB_2629482
Biological samples		
Patient-derived organoid line 60T	Calandrini et al., 2020	N/A
Patient-derived organoid line 60M	Calandrini et al., 2020	N/A
Patient-derived organoid line 78T	Calandrini et al., 2020	N/A
Patient-derived organoid line 103T	Calandrini et al., 2020	N/A
Patient-derived organoid line PMC-MRTK1	Calandrini et al., 2020	N/A
Patient-derived organoid line 33T	This paper	N/A
Patient-derived organoid line 51T	Calandrini et al., 2020	N/A
Patient-derived organoid line 86T	Calandrini et al., 2020	N/A
Patient-derived organoid line 80T	Calandrini et al., 2020	N/A
Patient-derived organoid line 68T	Calandrini et al., 2020	N/A
Patient-derived organoid line KK2	Hu et al., 2018	N/A
Patient-derived organoid line STE076	Drost et al., 2015	N/A
Patient-derived organoid line 60H	Calandrini et al., 2020	N/A
Patient-derived organoid line 78H	Calandrini et al., 2020	N/A
Patient-derived organoid line 103H	Calandrini et al., 2020	N/A
Chemicals, peptides, and recombinant proteins		
MLN4924 – neddylation inhibitor	MedChem Express	HY-70062
Sirolimus – mTOR inhibitor	MedChem Express	HY-10219
Doxorubicin	MedChem Express	HY-15142
Temsirolimus – mTOR inhibitor	MedChem Express	HY-50910
Collagenase	Sigma Aldrich	Cat# C9407
RhoKinase inhibitor Y-27632	Abmole Bioscience	Cat# M1817
EGF	Peprotech	Cat# AF-100-15
FGF10	Peprotech	Cat# 100-26
A83-01	Tocris	Cat# 2939/10
Advanced DMEM/F12	ThermoFisher Scientific	Cat# 12634010
B27 supplement	ThermoFisher Scientific	Cat# 17504044
BME	Trevigen	Cat# 3533-010-02

(*Continued on next page*)

Continued

REAGENT or RESOURCE	SOURCE	IDENTIFIER
GlutaMAX - L-alanine/L-glutamine	GIBCO	Cat# 35050061
HEPES	GIBCO	Cat# 15630106
N-acetylcysteine	Sigma Aldrich	Cat# A9165
Penicillin/Streptomycin	GIBCO	Cat# 15140163
Primocin - broad-range antibiotics	Invivogen	Cat# ant-pm-1
Critical commercial assays		
CellTiter-Glo 3D reagent	Promega	G9683
Deposited data		
RNA sequencing, Whole genome Sequencing 33T	This paper	EGA, EGAD00001007947; EGA, EGAD00001007948
DNA methylation 33T	This paper	GEO: GSE178737
RNA sequencing pediatric kidney tumors	Calandrini et al., 2020	EGA, EGAS00001003853
DNA methylation pediatric rhabdoid tumors	Chun et al., 2019	GEO: GSE123601
RNA sequencing SMARCB1 re-expression	This paper; Custers et al., 2021	EGA, EGAD00001007948; EGA, EGAD00001006574
Experimental models: Organisms/strains		
NOD-Scid IL2Rgnull mice	The Jackson Laboratory	JAX: 005557
Oligonucleotides		
See Table S5	This paper	N/A
Software and algorithms		
GraphPad Prism v7.04	GraphPad software	https://www.graphpad.com/
Kaluza analysis software v2.1	Beckman	https://www.beckman.com/flow-cytometry/software/kaluza
ImageJ	NIH	https://imagej.nih.gov/ij/
GSEA	Broad Institute	https://www.gsea-msigdb.org/gsea/index.jsp

RESOURCE AVAILABILITY

Lead contact

Further information and requests for resources and reagents should be directed to and will be fulfilled by the lead contact, Jarno Drost (J.Drost@prinsesmaximacentrum.nl).

Materials availability

This study did not generate new unique reagents.

Data and code availability

- Whole genome and RNA sequencing data have been deposited to the European Genome-Phenome Archive (https://ega-archive.org/ega/) under accession numbers EGA: EGAD00001007947 and EGA: EGAD00001007948. DNA methylation data has been deposited (https://www.ncbi.nlm.nih.gov/geo/) under accession number GEO: GSE178737.
- This paper does not report original code.
- Any additional information required to reanalyze the data reported in this paper is available from the Lead Contact upon request.

EXPERIMENTAL MODEL AND SUBJECT DETAILS

Animals

Mouse experiments were conducted in agreement with the Animal Welfare Committee of the Royal Netherlands Academy of Arts and Sciences, and the Netherlands Cancer Institute, the Netherlands. 8-12 weeks old NOD-Scid IL2Rgnull mice, 50% male and 50% females, were used as acceptors for subcutaneous injections of MRT organoids. Mice were stratified into groups without blinding. Sample sizes were calculated using statistical power analysis.

Patient-derived organoid lines

Experiments with human material were approved by the medical ethical committee of the Erasmus Medical Center (Rotterdam, the Netherlands) and Princess Máxima Center for Pediatric Oncology (Utrecht, the Netherlands). Informed consent was obtained from the parents of all participants (UMBRELLA and ITHER studies). Patient-derived organoids cultures have been established with protocols previously described and previously characterized (Calandrini et al., 2020). Briefly, rhabdoid tumor tissues were minced into 1 - mm^3 pieces, digested with collagenase (1 mg ml^{-1}, Sigma, C9407) supplemented with Rho-kinase inhibitor Y-27632 (10 μM, Abmole) for 45 minutes at 37°C. The digested tissue was washed with AdDF+++ and plated in factor-reduced BME (Trevigen, 3533-010-02). MRT and normal kidney organoids were cultured in BME, topped with kidney organoid medium (AdDF+++ supplemented with 1.5% B27 supplement (GIBCO), 10% R-spondin-conditioned medium, N-acetylcysteine (1.25 mM, Sigma), Rho-kinase inhibitor Y-27632 (10 μM, Abmole), FGF-10 (100 ng ml^{-1}, Peprotech), A83-01 (5 μM, Tocris Bioscience) and EGF (50 ng ml^{-1}, Peprotech) (Schutgens et al., 2019). Small intestinal and hepatocyte organoids lines have been cultured in conditions previously described (Drost et al., 2015; Hu et al., 2018).

METHOD DETAILS

Whole genome sequencing and RNA sequencing

Tissue and organoid samples derived from patient 33T have been processed, sequenced and analyzed following the INFORM pipeline (Worst et al., 2016). Briefly, whole genome sequencing was performed using 100ng of the Illumina adaptor-containing libraries produced with the Agilent Sureselect Version 5 protocol. RNA sequencing libraries were prepared with the TruSeq RNA Sample Preparation Kit v2 (Illumina) following the manufacturer's instructions. After library preparation all samples were 2x100bp paired-end sequenced on an Illumina HiSeq 4000. Whole genome read pairs were mapped to the 1000 Genomes Phase 2 assembly of the human reference genome (NCBI build 37.1) using the BWA aligner (version 0.6.2). RNA sequencing reads were mapped using the STAR algorithm version 2.3.0e onto the 1000 genomes reference sequence with Gencode version 17 transcript annotations. Whole genome sequencing coverage calculations considered all informative bases of the reference genome, excluding Ns, and were aggregated in 10kbp windows. Bulk RNA sequencing for *SMARCB1* re-expression line 33T has been performed and analyzed as previously described (Custers et al., 2021). Bulk RNA sequencing data from different sources (Calandrini et al., 2020; Schutgens et al., 2019) was merged and normalized counts were generated with the R-package DESeq2 using the *vst* function (Love et al., 2014). The 2500 most variable genes were used for a principal component analysis of which the 5 first components were used as an input for the tSNE function of the M3C R-package (John et al., 2020).

DNA methylation profiling

Tissue and organoid samples derived from patient 33T have been processed, sequenced and analyzed as previously described (Custers et al., 2021).

High throughput drug screening and validation

MRT organoids were digested into single cells 3 days prior to the screen. On the day of the screen, MRT organoids were harvested and washed in AdDF+++. Next, organoids were filtered using a 70 μm cell strainer (Falcon) and resuspended in 5% BME in kidney organoid medium. Afterward, ~500 organoids per well were plated using the Multi-drop^{TM} Combi Reagent Dispenser on repellent black 384-well plates (Corning) to which medium with compounds was added (6 different concentrations, 0.1nM to 10μM) using the Caliper Sciclone – Robotic Liquid Handling robot. Five days after drug addition, ATP levels were measured using CellTiter-Glo 3D (Promega) according to the manufacturer's instructions. Results were normalized to vehicle (100%). For the validation assays, 10 concentrations and 4 technical replicates were included. Drugs were dispensed with Tecan D300e Digital Dispenser. Normal kidney, small intestinal and hepatocytes organoids were prepared following the same protocol as for MRT organoids but plated in respective growth medium. AUC values were calculated with GraphPad Prism v7.04.

Regrowth assay

MRT organoids were dissociated, and 5000 single cells were seeded in 70% BME in kidney organoid medium with the addition of different drugs (Sirolimus (MedChem Express), MLN4924 (MedChem Express) and doxorubicin (MedChem Express)) or DMSO (Sigma-Aldrich). Three different plates have been prepared for the experiment. Cell viability was measured for the first plate with CellTiter-Glo 3D reagent (Promega) according to manufacturer's instructions (T0). Five days after, cell viability was assessed for a second plate (T5). At the same time, medium was changed for medium without drugs in the third plate. Five days after drug removal, cell viability was measured again (T10). Results were normalized to the DMSO control of T5 (100%).

Annexin V/DAPI double staining

Organoids were harvested and plated in 5% BME in kidney organoid medium and treated with either DMSO, MLN4924 50nM or Sirolimus 2nM. After 120h, organoids and supernatant were harvested. Organoids were dissociated into single-cell suspensions using TrypLE Express (Thermo Fisher) with the addition of Rho-kinase inhibitor Y-27632. Single-cell suspensions were stained with APC-AnnexinV (BD Biosciences, # 640920) and DAPI (Thermo Fisher, # D9542) in Annexin V binding buffer with the addition of 2.5mM

$Ca2^+$. Cells were acquired with Beckman Cytoflex LX flow cytometer. Data were analyzed with software Kaluza analysis v2.1. AnnexinV positive cell index was calculated by normalizing the percentages to DMSO controls.

Western blot

Western blot on organoids was performed as described (Drost et al., 2015). NEDD8 (Cell SignalingTechnology, #2754), βActin (Abcam, ab-6276), NAE1 (Thermo Fisher, #PA5-59836), UBE2M (Abcam, ab-109507), P21 (Santa Cruz, #SC6246), WEE1 (Santa Cruz, #SC5285) and GAPDH (Abcam, ab-9485) were used as primary antibodies.

Histology and immunohistochemistry

Tissues and organoids were fixed in 4% paraformaldehyde, dehydrated, and embedded in paraffin. Immunostaining was performed according to standard protocols on 4 μm sections. The following primary antibodies were used for immunohistochemical staining: NEDD8 (Cell Signaling Technology, #2754), Ki67 (Monosan, MONX10283), Cleaved caspase 3 (Cell Signaling Technology, #9661), NAE1 (Thermo Fisher, #PA5-59836) and UBE2M (Abcam, ab-109507). Imaging was performed using Leica DMi8 microscope.

3D immunofluorescence staining

Normal kidney and MRT organoids were disrupted into single cells. Three days later, organoids were harvested and plated in a chambered coverslip (IBIDI, #80826) in a slurry of 5% BME with the addition of DMSO or 50nM MLN4924. After 120h, samples were fixated and 3D imaging on organoids was performed as described (Dekkers et al., 2019). The following antibodies were used: Cleaved caspase 3 (Cell Signaling Technology, #9661), Alexa Fluor 647 phalloidin (Thermo Fisher, # A22287), DAPI (Thermo Fisher, # D9542). Imaging was performed using Leica SP8 microscope.

Resin electron microscopy

Organoids - cultured in 5% BME slurry with either DMSO or 50nM MLN4924 - were harvested after 48 hours and fixed in a mixture of 2% formaldehyde and 2.5% glutaraldehyde in 0.1M phosphate buffer pH 7.4 at room temperature for 2 hours. Afterward, organoids were rinsed and stored in 1% formaldehyde in 0.1M Phosphate Buffer pH 7.4 at 4°C overnight. Organoids were rinsed again with 0.1M Phosphate Buffer pH 7.4, and post-fixation was performed with 1% OsO4, 1.5% K3Fe(III)(CN)6 in 1M Phosphate Buffer PH 7.4 for 2 hours. Organoids were then dehydrated in a series of acetone (70% overnight, 90% 15 min, 96% 15 min, 100% 3x 30 min), and embedded in Epon (SERVA). Ultrathin sections of 65 nm were cut (Leica Ultracut UCT), collected on formvar and carbon coated TEM grids and stained with uranyl acetate and lead citrate (Leica AC20). Micrographs were collected on a JEM1010 (JEOL) equipped with a Veleta 2k × 2k CCD camera (EMSIS, Munster, Germany) or on a Tecnai12 (FEI Thermo Fisher) equipped with a Veleta 2k × 2k CCD camera (EMSIS, Munster, Germany) and operating SerialEM software.

RNA isolation, cDNA preparation, and qRT-PCR

Organoids were harvested in RLT lysis buffer and RNA was isolated using the QIAGEN RNeasy kit (QIAGEN) following manufacturer's instruction. The extracted RNA was used for cDNA production using GoScript reverse transcriptase (Promega) following manufacturer's instructions. qRT-PCR was performed using IQ SYBR green mix (Biorad) following manufacturer's instructions. Results were calculated using the ΔΔCt method. Primer sequences: NOXA_FW (GTGTGCTACTCAACTCAG), NOXA_RV (ATTCCTCTCAATTA CAATGC) (Drost et al., 2010), P21_FW (TACCCTTGTGCCTCGCTCAG), P21_RV (GAGAAGATCAGCCGGCGTTT) (Drost et al., 2015), WEE1_FW (ATTTCTCTGCGTGGGCAGAAG), WEE1_RV (CAAAAGGAGATCCTTCAACTCTGC) (Wang et al., 2016), BIM_FW (ATGTCTGACTCTGACTCTCG), BIM_RV (CCTTGTGGCTCTGTCTGTAG) (Delannoy et al., 2018), CHOP_FW(ACCAAGGGAGAAC CAGGAAACG),CHOP_RV(TCACCATTCGGTCAATCAGAGC) (Toral et al., 2017), GAPDH_FW(TGCACCACCAACTGCTTAGC), GAPDH_RV(GGCATGGACTGTGGTCATGAG) (Vandesompele et al., 2002).

In vivo drug study

250 000 small size MRT organoids were harvested and implanted subcutaneously in the right flank of NOD-Scid IL2Rgnull mice, in a solution 1:1 with BME. When tumors reached approximately $250mm^3$, mice were randomized to MLN4924 (n = 12 mice), Temsirolimus (n = 9 mice) or respective vehicles. MLN4924 (60mg/kg) or vehicle (10% cyclodextrin) were injected subcutaneously twice daily for 35 days (5 cycles of 5 days on, 2 days off). Temsirolimus (5mg/kg) or vehicle (saline) were administered via intraperitoneal injection once a day for 42 days (6 cycles of 5 days on, 2 days off). Tumor volume was monitored 3 times a week by caliper measurement. When reaching halfway and the end of the treatment, 3 mice per arm were sacrificed for histological analysis of the tumors and organs. The other 9/6 mice were kept for survival studies. Mice were sacrificed when reaching humane endpoint (tumor > 1500 mm^3).

QUANTIFICATION AND STATISTICAL ANALYSIS

For comparison between two sample groups, statistical analysis was conducted using the two-tailed unpaired Student's t tests. All statistical data can be found in the figure legends.